BBA - General Subjects 1862 (2018) 2824–2834

Contents lists available at ScienceDirect

BBA - General Subjects

journal homepage: www.elsevier.com/locate/bbagen

Supramolecular zippers elicit interbilayer adhesion of membranes producing cell death

Víctor G. Almendro-Vedia[a,b], Carolina García[c], Rubén Ahijado-Guzmán[a], Diego de la Fuente-Herreruela[a,b], Mónica Muñoz-Úbeda[b], Paolo Natale[a,b], Montserrat H. Viñas[d], Rodrigo Queiroz Albuquerque[e,f], Andrés Guerrero-Martínez[a], Francisco Monroy[a,b], M. Pilar Lillo[c], Iván López-Montero[a,b,*]

[a] Dto. Química Física, Universidad Complutense de Madrid, Avenida Complutense s/n, 28040 Madrid, Spain
[b] Instituto de Investigación Hospital Doce de Octubre (i+12), Avenida de Córdoba s/n, 28041 Madrid, Spain
[c] Dto. Química Física Biológica, Instituto de Química-Física "Rocasolano" (CSIC), Serrano 119, 28006 Madrid, Spain.
[d] ETS de Sistemas Informáticos, Universidad Politécnica de Madrid, Alan Turing s/n, 28031 Madrid, Spain
[e] School of Pharmacy and Biomolecular Sciences, Liverpool John Moores University, L3 3AF Liverpool, United Kingdom
[f] São Carlos Institute of Chemistry, University of São Paulo (USP), 13566-590 São Carlos, Brazil

ARTICLE INFO

Keywords:
Fibroblasts
Mitochondria
Giant vesicles
H-aggregate
NAO

ABSTRACT

Background: The fluorescent dye 10-*N*-nonyl acridine orange (NAO) is widely used as a mitochondrial marker. NAO was reported to have cytotoxic effects in cultured eukaryotic cells when incubated at high concentrations. Although the biochemical response of NAO-induced toxicity has been well identified, the underlying molecular mechanism has not yet been explored in detail.

Methods: We use optical techniques, including fluorescence confocal microscopy and lifetime imaging microscopy (FLIM) both in model membranes built up as giant unilamellar vesicles (GUVs) and cultured cells. These experiments are complemented with computational studies to unravel the molecular mechanism that makes NAO cytotoxic.

Results: We have obtained direct evidence that NAO promotes strong membrane adhesion of negatively charged vesicles. The attractive forces are derived from van der Waals interactions between anti-parallel H-dimers of NAO molecules from opposing bilayers. Semi-empirical calculations have confirmed the supramolecular scenario by which anti-parallel NAO molecules form a zipper of bonds at the contact region. The membrane remodeling effect of NAO, as well as the formation of H-dimers, was also confirmed in cultured fibroblasts, as shown by the ultrastructure alteration of the mitochondrial *cristae*.

Conclusions: We conclude that membrane adhesion induced by NAO stacking accounts for the supramolecular basis of its cytotoxicity.

General significance: Mitochondria are a potential target for cancer and gene therapies. The alteration of the mitochondrial structure by membrane remodeling agents able to form supramolecular assemblies via adhesion properties could be envisaged as a new therapeutic strategy.

1. Introduction

10-*N*-nonyl acridine orange (NAO) is a lipophilic fluorescent dye comprising an acridine derivative nitrogen heterocycle bound to a nonyl acyl chain (Fig. 1a). NAO presents a maximum emission wavelength at λ_{em} = 525 nm that shifts to 640 nm at high concentrations due to the planar geometry of the acridine molecule and its aggregation or molecular stacking behavior [1]. Indeed, the aggregation of acridine

Abbreviations: 2P-FLIM, two-photon fluorescence-lifetime imaging microscopy; AO, acridine orange; ATP, adenosine triphosphate; CL, cardiolipin; DFT, density functional theory; DMEM, Dulbecco Modified Eagle Medium; E_{adh}, adhesion strength; *E. coli*, *Escherichia coli*; GP, generalized polarization; GUV, giant unillamelar vesicle; IMM, inner mitochondrial membrane; ITO, indium tin oxide; LUV, large unilamellar vesicle; KCl, potassium chloride; MEF, mouse embryonic fibroblasts; NAO, 10-*N*-nonyl acridine orange; PE, phosphatidylethnolamine; POPC, 1-palmitoyl-2-oleoyl-*sn*-glycero-3-phosphocholine; PLE, polar lipid extract; POPG, 1-palmitoyl-2-oleoyl-*sn*-glycero-3-phosphoglycerol; SA, stearic acid; TD-DFT, time-dependent DFT; κ, bending rigidity; σ, surface tension

* Corresponding author.
E-mail address: ivanlopez@quim.ucm.es (I. López-Montero).

https://doi.org/10.1016/j.bbagen.2018.08.018
Received 7 May 2018; Received in revised form 3 August 2018; Accepted 27 August 2018
Available online 30 August 2018

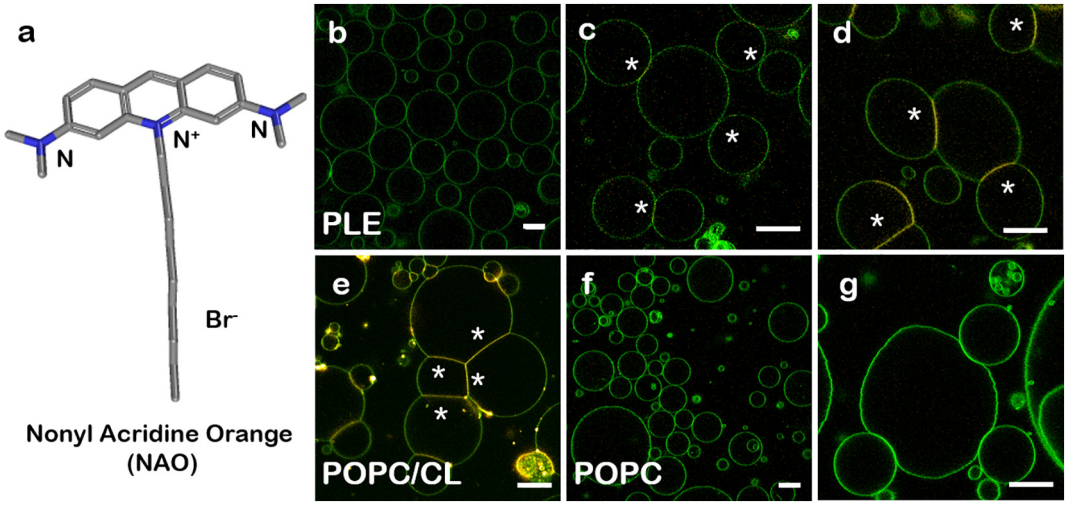

Fig. 1. NAO-promoted interbilayer adhesion of negatively-charged lipid vesicles. (a) Chemical structure of NAO. **(b–g)** Confocal fluorescence micrographs of NAO-stained GUVs composed of either *E. coli* PLE (b–d), POPC/CL (60/40 wt%) (e) or pure POPC (f–g). Green channel (λ_{exc} = 488 nm) and red channel (λ_{exc} = 561 nm). Low concentration of NAO did not promote vesicle adhesion in *E.coli* PLE GUVs whereas high concentrations of NAO elicited vesicle adhesion in both *E.coli* PLE (c–d) and POPC/CL GUVs (e). Note the red shift fluorescence emission at contact sites (white stars). Conversely, NAO did not cause either vesicle adhesion or the green-to-red emission shift in pure POPC vesicles (f–g). Time lapse between (c) and (d) was 30 s. The final concentration of NAO was 5 nM (b) or 25 μM (c–g). Scale bars are 10 μm.

results from π–π interactions between stacked molecules, as demonstrated for the binding of acridine orange to nucleic acids [2]. Similarly, the observed green-to-red emission shift has been interpreted as a consequence of NAO-NAO self-interactions when embedded in cardiolipin (CL)-enriched lipid membranes [1,3,4].

Its molecular hydrophobic character enables NAO to diffuse spontaneously into membrane environments, and thus the use of NAO as a stain for inner mitochondrial membranes (IMMs) is widely expanded [5–7]. The negative membrane potential of mitochondria allows the cationic lipophilic dye to enter and accumulate within the mitochondrial matrix. In addition, the mechanism by which NAO specifically binds IMMs was suggested to occur by means of its specific interaction with CL [1,3,4]. IMMs and bacterial membranes share a similar lipid composition [8,9], in particular their high content in both phosphatidylethnolamine (PE) and the negatively charged lipid CL. Thus, NAO has been considered the canonical fluorescent dye to reveal CL domains also in *Escherichia coli* membranes [10,11].

NAO is routinely used as a mitochondrial dye; however, its incubation with eukaryotic cells at high micromolar concentrations induces cytotoxicity [12]. The accumulation of NAO in IMMs inhibits cellular respiration, eventually triggering the alteration of the mitochondria morphology [12]. In particular, NAO inhibits the oxygen consumption, the activity of respiratory complexes and ATP synthesis [7]. To date, there is no explanation for the molecular mechanism of such NAO inhibitory effects. The specific interaction with CL hints to possible physical interactions of the dye with its lipidic environment as the basis for the NAO cytotoxicity. Although it has been reported that increasing NAO concentrations and incubation times promote the transformation of the mitochondrial *cristae* into multi-lamellar stacked membranes and the final collapse of the mitochondria [12], the direct impact of NAO on membrane remodeling has not been explored to date.

Here, we unveil the supramolecular mechanism underlying the NAO cytotoxicity. First, we confirmed the membrane shaping effect of NAO on giant unillamelar vesicles (GUVs) composed of CL and other negatively charged lipids. We present evidence that NAO mediates the adhesion of lipid bilayers with an adhesion strength of $E_{adh} \approx 10^{-6}$ J/m^2. Fluorescence lifetime imaging microscopy (FLIM) revealed the presence of long-lifetime H-dimers formed by NAO molecules from opposing adhering bilayers localized at the contact region. Computational calculations using semi-empirical methods confirmed this picture. The incubation of mammalian cells with NAO elicited cytotoxicity with global morphological changes including blebbing and cell shrinkage via the formation of NAO H-dimers. A detailed analysis of the mitochondrial ultrastructure of NAO-incubated cells confirmed the morphological alteration of the *cristae*. We conclude that the supramolecular assembly of NAO dimers from adjacent membranes results in the cytotoxic effect of NAO by inducing serious mechanical modifications in the IMM. Our results are relevant for the design and set-up of alternative strategies to control the proliferation and viability of cells by modulating the mechanical properties of IMMs.

2. Materials and methods

2.1. Chemicals

Potassium chloride (KCl), glucose, sucrose, and glycine were purchased from Sigma-Aldrich. NAO was supplied by Thermofisher. Ultrapure water was produced from a Milli-Q unit (Millipore, conductivity below 18 MΩ cm).

2.2. Lipids

1,2-dioleoyl-sn-glycero-3-phosphoethanolamine (DOPE), 1-Palmitoyl-2-oleoyl-*sn*-glycero-3-phosphocholine (POPC), CL from *E.coli*, 1-palmitoyl-2-oleoyl-*sn*-glycero-3-phosphoglycerol (POPG), and *E coli* polar lipid extract (*E.coli* PLE) were supplied by Avanti Polar Lipids and suspended in chloroform at 1 mg/mL (DOPE, POPC, CL and POPG) or 20 mg/mL (*E.coli* PLE). According to the manufacturer, the composition of the *E.coli* PLE is 67% wt PE, 23.2% wt PG and 9.8% wt CL. Lipids were stored at −20 °C.

2.3. Electroformation of giant unilamellar vesicles

Giant vesicles were prepared using the standard electroformation protocol [13]. The fabrication chamber was composed of two 1-mm spaced conductor indium tin oxide (ITO)-coated slides (7.5 × 2.5 cm^2, 15–25 Ω/sq surface resistivity; Sigma). *E.coli* PLE GUVs were prepared by transferring two 5-μL drops of 20 mg/mL *E.coli* PLE to each ITO slide. After solvent evaporation, the fabrication chamber was sealed using *V*itrex paste (Vitrex Medical, Herlev, Denmark). Then, the films

were rehydrated in sucrose solution (200 mM) and the electrodes were connected to an AC power supply (Agilent, 500 Hz, 1.1 *V*) for at least 3 h. To prepare POPC, POPC/CL, POPC/POPG and POPC/DOPE/CL GUVs, two 5-μL drops at 1 mg/mL were transferred to each ITO slide. The electroformation conditions in those cases were 8 Hz at 1.1 V for POPC and 500 Hz at 1.1 V for POPC/CL POPC/POPG and POPC/DOPC/CL.

2.4. Large unilamellar vesicles (LUVs)

LUVs made of *E. coli* PLE were obtained by extrusion [14]. Briefly, 50 μL of *E.coli* PLE (20 mg/mL) were evaporated under vacuum yielding a homogenous lipid film consisting of multiple lamellae. The lipid film was then hydrated with water (1 mg/mL final lipid concentration). During the hydration phase the dispersion was repeatedly vortexed. The lipid suspension was then extruded 11 times through a polycarbonate filtering membrane (Whatman, Florham Park, NJ) with a 100 nm pore size. NAO was externally incorporated at desired concentrations and the absorption spectra and fluorescence spectra were recorded at 20 °C with a Genesis 10 spectrophotometer (Fisher scientific, spectral bandwidth of 1.0 nm and a scan rate of 200 nm/min) and with an AMINCO-Bowman Series 2 (AB2) Spectrofluorometer respectively.

2.5. Cell cultures

Mouse embryonic fibroblasts (MEF) (3T3NIH; purchased from ATCC) were cultured in Dulbecco Modified Eagle Medium (DMEM), 25 mM glucose (Gibco) supplemented with 10% fetal bovine serum (South Africa S1300; Biowest, Nuallé, France), penicillin/streptomycin (final concentration 100 U/mL of penicillin and 100 μg/mL of streptomycin), and 1% of non-essential amino acids (all Gibco). The cells were grown in a humidified incubator (Forma Steri-Cycle Themofisher; 5% CO2) at 37 °C and maintained with a split ratio of 1:10 at 80% of confluence in T75 flasks (Nunc).

2.6. Confocal microscopy

Confocal microscopy images of GUVs were collected at 20 °C with a Nikon Ti-E inverted microscope equipped with a Nikon C2 scanning confocal module, 488 and 561 nm continuous lasers, emission bandpass filters, and a Nikon Plan Apo 100× NA 1.45 oil immersion objective. For GUV observation, 20 μL of GUVs were diluted in 80 μL of glucose solution (200 mM). The GUVs sedimented after 15 min. Then, 0.5 μL of NAO (5 nM–25 mM final concentration) was added to the vesicles. For cell observation, MEFs were seeded at 2.5×10^5 cells per cm^2 in a four-chamber Lab-Tek® slide (Thermofisher) and incubated with complete high glucose DMEM for 24 h at 37 °C. Prior to confocal fluorescence imaging, MEFs were supplemented with NAO (5 nM or 5 μM) and the Lab-Tek® slide was mounted on the temperature (37 °C) controlled stage.

2.7. Two-photon generalized polarization imaging

Two-photon generalized polarization imaging (GP) was used here as a simple approach to quantitatively analyze the differences between pairs of fluorescence intensity images (*I#1*, *I#2*) measured simultaneously in two emission regions, the red channel (#1; 685 nm) and green channel (#2; 520 nm) with two-photon excitation at 850 nm, using the MicroTime 200 system described below. The emission (FF01 520/35 and FF01 685/40) and dichroic FF560-Di01 filters were from Semrock, Germany. The difference between both intensity images was effectively normalized by dividing by their sum to give a unit-less image defined by [15]

$$\mathrm{GP} = \frac{I\#2 - I\#1 \times G}{I\#2 + I\#1 \times G} \tag{1}$$

For the spectral conditions used in this work, the estimated *G* factor value was 0.5. However, with the aim of increasing the contrast between the red and green emission regions, we used in this work an effective *G* factor value of 1.0, and thus the GP values provided here should be considered only qualitatively. In any case, negative values (green color) would correspond to a greater proportion of red-aggregated NAO species, and, in the same way, positive values (magenta color) would correspond to a greater proportion of monomer NAO species in the magenta/green color gradient scale.

2.8. Two-photon fluorescence lifetime imaging

Two-photon, two-color (red and green) fluorescence-lifetime imaging (2P-FLIM) of *XY* sections of GUVs and cells was carried out on a MicroTime200 system (PicoQuant, Germany) equipped with a mode-locked, femtosecond-pulsed Ti:Sapphire laser (Mai-Tai, Spectra Physics, CA) operating at a repetition rate of 80 MHz, circularly polarized and tuned to 850 nm. The set-up consists on an Olympus IX71 inverted microscope mounted with a 60× water-immersion objective NA1.2; a piezo *XY*-scanning table and two single-photon counting avalanche diodes (*τ*-SPAD, PicoQuant, Germany), and a PicoHarp 300 PC-board (PicoQuant, Germany), synchronized with the excitation laser pulses using the Time-Tagged Time-Resolved (TTTR) detection mode at 23 °C. The TTTR mode allows the recording of every individual fluorescence photon from each pixel, together with its timing and emission color (#1, #2). The acquisition time per pixel accounted for 0.6–1.2 ms, resulting in an overall image acquisition time of 60–180 s, depending on the image resolution and intensity of the fluorescence signal. For each image, all the detected photons per pixel were used to build steady-state fluorescence intensity images or Fast FLIM and FLIM phasor images. For this, we use the ps-temporal resolution of the system, SymphoTime 64 software (Fast FLIM; PicoQuant, Germany), and SimFCS software (Phasor Analysis) developed at the Laboratory of Fluorescence Dynamics (LFD, UC Irvine). The filters used in this study were all from Semrock (Germany). Red channel (#1): FF01-685/40; green channel (#2): FF01–520/35; with a dichroic beam splitter FF560-Di01. Although in the red channel #1 we mostly select red NAO aggregates, a non-negligible bleedthrough from NAO green monomers may exist, particularly when the monomer NAO population is the majority. The excitation power was lower than 1 mW at the sample, and it was adjusted using a variable optical attenuator LS-107AT (Lasing, S.A. Spain) to achieve counting rates below 10^6 photons/s. In the phasor plot, the effect of the instrumental response function (IRF) on the calculated phasor coordinates was taken into account by using the fluorescence decay of a standard fluorophore of known lifetime, measured in the same experimental conditions as the sample, as a reference. In this way, we get the correct scale for the calculated phasor coordinates in the phasor plot.

2.9. Adhesion energy density quantification

We measured the adhesion energy density of *E.coli* PLE GUVs from the overall shape of adhered doublets and following the protocol described in ref [16]. Briefly, for each adhesion event, we acquired confocal images of the equatorial cross-sections. Images were processed with the Nikon NIS-Elements software and the doublet contour was then identified with a homemade software (MATLAB R2013b, The MathWorks Inc.). Assuming that the shapes were axisymmetric, we first measured the enclosed volume V_i and the total membrane area A_i of each adhering vesicle by integration along their contour (see Fig. 4a), where $i = 1,2$ stands for each vesicle forming the doublet. In the strong adhesion regime, the contact angle $\theta_0{}^i$ is numerically determined by the reduced volume $\frac{V_i}{A_i^{2/3}}$ according to:

$$\frac{V_i}{A_i^{2/3}} = \frac{8 - 9\cos\theta_0^i + \cos 3\theta_0^i}{12\sqrt{\pi}(2 - 2\cos\theta_0^i + (\sin\theta_0^i)^2)^{3/2}} \tag{2}$$

The radius of the circular contact area in the strong adhesion regime, R_0^i, is determined by:

$$R_0^i = \sqrt{\frac{A[1+\cos\theta_0^i]}{\pi[3+\cos\theta_0^i]}} \quad (3)$$

Finally, the adhesion energy densities E_{adh} were calculated from the contact radius $R_0{}^i$ and contact angles $\theta_0{}^i$ of adhering vesicles [16,17].

$$E_{adh}^i \approx \frac{2\kappa}{(R-R_0^i)^2}\left(\frac{\cos(\theta_0^i/2)}{1+\sin(\theta_0^i/2)}\right)^2 \quad (4)$$

where κ is the bending rigidity and R is the actual radius of the adhering membrane segment as measured directly from images. This procedure was repeated for each adhesion event, thus obtaining an averaged adhesion energy density of all the adhesion events.

2.10. Bending rigidity of E.coli PLE GUVs

We measured the bending rigidity of *E.coli* PLE GUVs by fluctuation analysis of the thermally induced motion of the membrane. Membrane fluctuations were enhanced by osmotic shock (250–300 mOsm glucose) and recorded at 22 °C. Experiments were performed on an inverted Nikon Eclipse 2000Ti (Nikon, Japan) microscope equipped with a 100 W TI- 12 DH Pillar Illuminator, an LWD 0.52 collimator, and a PlanApo VC 100× (NA1.4) oil immersion objective. Images were captured with a FASTCAM SA3 camera (Photron, San Diego, CA, USA) using an effective pixel-size of 50 nm × 50 nm at 500 frames per second to provide images with an optimal signal-to-noise ratio (SNR). The GUV contours were automatically tracked at the equatorial plane with a custom-made algorithm [18]. The description of the normal deformation h in a series of discrete Fourier modes, $h(t) = \Sigma_{(q)} h_q(t)$ exp.(iqx), allowed the calculation of the fluctuation spectrum $P(q)$,

$$P(q) = \frac{k_B T}{(\sigma q^2 + \kappa q^4)} \quad (5)$$

where $q = l/R$ is the equatorial projection of the fluctuation wavevector (with R as the radius and $l = 2, 3, 4, \ldots \infty$ the azimuthal number), κ is the bending rigidity, and σ is the surface tension. The mechanical parameters κ and σ were obtained by fitting the experimental mode amplitudes to the theoretical fluctuation spectrum $P(q)$ particularized to the equatorial fluctuations [19].

2.11. Theoretical calculations

Density Functional Theory (DFT), Time-Dependent DFT (TD-DFT), and semi-empirical calculations at the dispersion-corrected PM6 level [20] were carried out using the Gaussian09 and MOPAC2016 packages respectively. The DFT and TD-DFT calculations were performed at the PBE0/6-31G* level [21]. All calculations were carried out in vacuum. The molecular structures of CL and NAO were drawn using the AVOGADRO program and their geometries were fully optimized at the semi-empirical level without any geometrical constraints. The insertion of water molecules in the CL-NAO system is not trivial, since a simulation box with periodic boundary conditions would need to be built, which is out of the scope of this work. However, the aim of these calculations was to investigate the stability of the final structure containing CL-NAO after adhesion between the polar parts of two different bilayers, and the amount of water at the bilayer-bilayer interface after adhesion was expected to be very small. Although this might be a limitation of our theoretical method, meaningful insights can still be drawn from the corresponding results, as we indeed show in this work. The absence of negative (complex) vibrational frequencies was used to confirm the reliability of the optimized geometries. Heats of formation were calculated using the above PM6 method, while UV–Vis spectra were predicted using the ZINDO/S model [22] implemented in the ORCA package [23] and adopting the PM6-optimized geometries.

2.12. TEM imaging

TEM images were obtained with a JEOL JEM-1010 transmission electron microscope operating at an acceleration of 80 kV (CNME, Spain). The cells were incubated with NAO at different concentrations for 60 min, washed, and fixed with 2% glutaraldehyde in phosphate buffered saline solution (PBS). Then, they were stained with 1% osmium tetroxide and 1.5% potassium cyanoferrate and gradually dehydrated in acetone. The samples were embedded in Epon and cut by ultramicrotomy into 60 nm sections for observation.

3. Results

3.1. NAO-promoted interbilayer adhesion of negatively charged lipid vesicles

To explain the cytotoxic effect of NAO in eukaryotic cells, we first explored the action of the dye on the mechanical properties of model membranes built as electroformed GUVs. As IMMs are similar in lipid composition to the membranes of bacteria [8,9], we used a *E.coli* PLE to mimic the IMM lipid composition. The electroformed *E.coli* PLE vesicles were spherical, with a variable size ranging from a few up to several tens micrometers [18]. Upon NAO incubation (25 μM final concentration), the lipid bilayer was fluorescently stained (green), as observed by confocal fluorescence microcopy (Fig. 1b). Vesicles started to adhere in single and multiple events as they came into close contact. Upon vesicle adhesion, we observed an increase of the NAO specific red fluorescence at the contact sites of adhered GUVs (Fig. 1c-d). Similar observations were made in mixed palmitoyl-oleoyl-phosphatidylcholine POPC/CL vesicles (from 90/10% wt up to 60/40% wt), as shown in Fig. 1e. Control GUVs made of pure POPC did not display any significant adhesion or fluorescence at the membrane surface in the red channel (Fig. 1f and Fig. 1g). At high concentration of NAO (up to 1 mM) we observed the green-to-red fluorescence shift of the dye but POPC vesicles did not adhere (Supplementary Fig. 1a). This suggests that the presence of CL is a requirement for membrane adhesion. Likewise, we observed similar adhesion kinetics for GUVs made of POPC and POPG (POPC/POPG from 90/10% wt up to 60/40% wt). PG is a negatively charged lipid and a common precursor for the de novo biosynthesis of CL in cells. This result is consistent with previous reports describing the specific interactions of NAO with negatively charged lipids [24]. Remarkably, below 10 nM, NAO did not trigger vesicle adhesion, pointing to the requirement of a NAO concentration threshold to induce interbilayer interactions.

To rule out that the observed membrane adhesion could be mediated by electrostatic interactions between the cationic charge of the NAO nitrogen heterocycle and the negative phosphates of CL, we incubated *E.coli* PLE GUVs in the presence of a salt (KCl 100 mM). Under these conditions, we still observed vesicle adhesion despite the electrostatic screening that occurs under high ionic strength conditions (see Supplementary Fig. 1b). Similar results were obtained when POPC/CL vesicles were incubated at pH = 3 (200 mM glycine buffer), well below the pK_1 of CL [25] (Supplementary Fig. 1c). At this pH, CL does not bear a negative charge on the headgroup and therefore, the observed interbilayer interactions cannot be solely electrostatic in nature. Finally, NAO also promoted vesicle adhesion on IMM-mimicking GUVs made on POPC/DOPE/CL (45/35/20% wt). This composition was chosen according to [26] (Supplementary Fig. 1d). The GUV adhesion in all the above experiments indicated the presence of strong intermolecular van der Waals-like attractive forces between NAO molecules in the presence of CL or other negative lipids. This type of interaction is frequently encountered in fluorescent dye self-association. Stacked dyes exhibit distinct changes in the absorption and emission bands compared to those of monomeric species. Thus, the red-shifted fluorescence at the contact region in adhering vesicles strongly supports direct interbilayer interactions of supramolecular assemblies of NAO molecules.

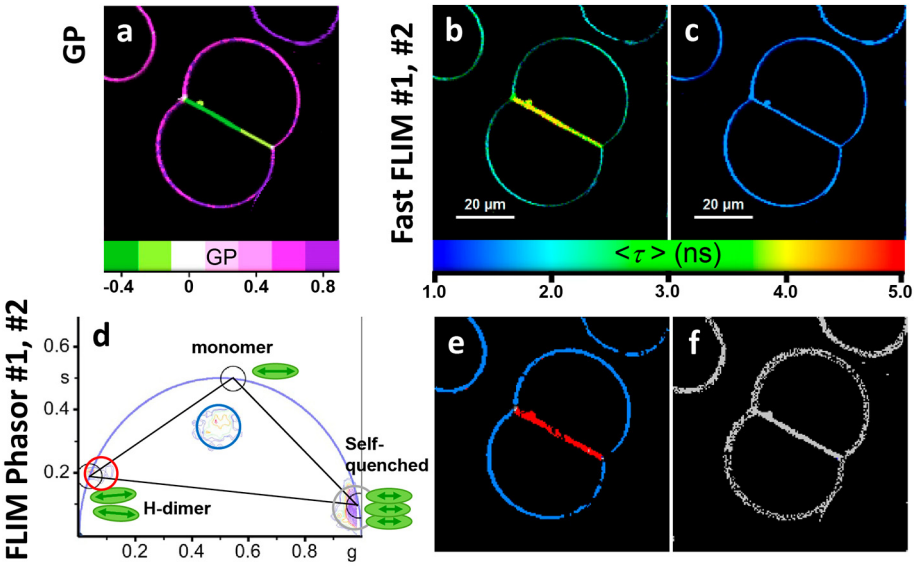

Fig. 2. Spatial distribution of NAO molecular species in PLE vesicles. *XY* sections determined at the equator of representative groups of *E.coli* PLE GUVs treated with 5 µM NAO. **(a)** Generalized Polarization GP image and **(b** and **c)** intensity-weighted Fast FLIM images of the same group of GUVs, acquired simultaneously at two emission regions, the red (#1) and green (#2) channels. Phasor Analysis: **(d)** Phasor plot showing the phasor cluster locations corresponding to regions enriched in long-lifetime NAO antiparallel H-dimers (red cursor; as detected in channel #1), intermediate-lifetime NAO monomers (blue cursor; as detected in channel #1), and short-lifetime self-quenched NAO aggregates (grey cursor; as detected in channel #2). Black cursors on the phasor plot represent 100% pure NAO species: NAO antiparallel H-dimers (τ = 10 ns), monomeric NAO (τ = 1.8 ns), and self-quenched NAO aggregates (τ = 0.2 ns). Black solid lines joining the three pure species phasors form a triangle that would contain phasors from all possible intensity-weighted combinations of the three NAO molecular species. **(e** and **f)** Lifetime color maps of NAO molecular species at two emission regions, the red channel (#1) and green channel (#2). Pixels corresponding to the cluster of phasors enclosed by the colored circles are highlighted on the intensity image using the same color. GP false color green-white-blue violet scale (−0.5, +0.9): Green to blue-violet colors highlight regions showing higher to lower red/green emission ratios for the NAO species, respectively. Fast FLIM rainbow color scale (1–5 ns): λ_{exc} = 850 nm, red channel (#1) FF01 685/40, green channel (#2) FF02 520/35, dichroic filter FF560-Di01 (Semrock, Germany), 1.2 ms/pixel. (For interpretation of the references to color in this figure legend, the reader is referred to the web version of this article.)

3.2. Long excited-state lifetime molecular species of NAO accumulate in the contact region of adhered vesicles

To further examine the red-shifted fluorescence exhibited by NAO molecules at the contact region of adhering vesicles made of PLE, we first used the Intensity Generalized Polarization (GP) approach. GP images were calculated from the steady-state fluorescence images recorded simultaneously at two emission regions, red (#1), and green (#2), using Eq. (1) (see Materials and Methods). This method provides a simple and quantitative graphical way of comparing the spatial distribution of red and green NAO fluorescence intensities. As shown in Fig. 2a, the aggregated NAO molecules (red fluorescence molecular species) concentrate at the septa of the adhering vesicles, whereas the fluorescent probes from the green channel (#2) accumulate in non-adhering regions.

Next, we performed time-resolved fluorescence imaging experiments to distinguish NAO molecular species by their excited-state lifetimes. Figs. 2b–f shows the two-photon fast FLIM and FLIM-phasor images of a representative group of two adhered *E.coli* PLE GUVs (see Fig. S2 for other examples) measured in the two emission regions, (#1) and (#2). Fast FLIM (#1) images show longer average excited-state lifetimes ($<\tau>$) at the contact region of adhering GUVs, whereas Fast FLIM (#2) images show a nearly uniform distribution of short average lifetime species. Fast FLIM images obtained with the SymphoTime software (PicoQuant, Germany) use the average photon arrival time per pixel as an indicator of the intensity averaged excited-state lifetime. Note that when the experimental time window is of the same order of magnitude as the fluorophore lifetimes, the average lifetimes determined from Fast FLIM are always found to be lower than the true value. Here, we used Fast FLIM images only in a qualitative way to discriminate regions of interest enriched in the different NAO molecular species (see Materials and Methods). A detailed global analysis of the picosecond time-resolved decays from different regions of interest (ROIs) by a multi-exponential function revealed the existence of three NAO molecular species with excited-state lifetimes of 10, 1.8, and 0.2 ns. The 10-ns lifetime NAO species was only detected in the red channel #1; whereas the 1.8-ns and 0.2-ns NAO species were detected in both emission channels, but mainly in the green channel #2. To better localize and quantify the different lifetime species, we used the FLIM-phasor approach for the three-species system (Fig. 2d) with excited-state lifetimes of 10, 1.8, and 0.2 ns lying on the universal circle (black cursors). The 1.8-ns lifetime coincides with the measured lifetime of monomeric NAO in ethanol solution (data not shown). Phasors from non-adhering regions in channel #1 (Fig. 2d and e, blue color) correspond to a mix of the three species enriched in the 1.8-ns species, as indicated by the location of the corresponding cluster of phasors inside the three species triangle [27]. Phasors from contact adhering sites contain nearly pure 10-ns NAO species (Fig. 2d and e, red color). A ubiquitous species with a very short fluorescence lifetime of 0.2 ns was detected in channel #2 (Fig. 2d and f, grey color). This molecular species was not detected at nanomolar concentrations of NAO (data not shown), pointing out the existence of a concentration threshold for this particular NAO species that may correspond to NAO molecules close enough to self-quench but not to red-shift. As a consequence, their fluorescence lifetime significantly decreases. The self-quenching of NAO in solution has been already reported as increased self-absorption and decreased fluorescence intensity accompanied with a minor emission red-shift [1,28] (Supplementary Fig. 3).

3.3. NAO molecules from different lipid bilayers form H-aggregates

The spectroscopic properties of supramolecular aggregates depend strongly on the mutual orientation of the monomers. Based on Single Exciton Theory [29], two kind of dimers can be formed, exhibiting distinct changes in the absorption and emission bands relative to those of the monomeric species. When monomers undergo a head-to-tail arrangement, the so-called J-aggregates show a red-shifted narrow absorption band and generally display enhanced fluorescence. In contrast, H-aggregates are formed by the parallel (head-to-head) arrangement of dyes, exhibiting a blue-shifted absorption band and behaving as non-fluorescent dimers [30,31]. Although H-aggregates are ideally non-fluorescent, intermediate arrangements can occur when dipoles form twisted H-aggregates. The imperfect stacking may result in partially allowed transitions responsible for the observed H-aggregate fluorescence [32–34].

Supplementary Fig. 4 shows the UV–Vis absorption and fluorescence emission spectra of NAO at low concentration (500 nM) in aqueous solution. According to the literature, NAO displays a broad band in

the 450–540 nm region with a maximum at 495 nm, along with a shoulder at around 470 nm [1,3,4,35]. The 495-nm band corresponds to monomer NAO absorption in solution and the weak shoulder at 470 nm corresponds to dimeric arrangements of NAO in solution [1,3,4,35]. In the presence of *E.coli* PLE large unilamellar vesicles (LUVs), two different behaviors are observed. At low NAO/CL ratios (NAO/CL = 0.2), neither the absorption nor the fluorescence emission (λ_{max} = 520 nm) show remarkable differences when compared to the NAO spectrum in aqueous buffer. However, at NAO/CL = 2, the intensity of the monomer band decreases concomitantly with a more intense dimeric band [1,3,4]. This is also reflected in the fluorescence emission spectrum with the appearance of a second fluorescence emission band at 620 nm, as previously reported [24]. This dimer has been assigned as a H-dimer for acridin orange molecules and their lipophilic derivatives when embedded in different media such as polymers or aliphatic interfaces [36,37]. The observation of red-shifted fluorescence suggests the formation of twisted face-to-face H-dimers.

Quantum chemical calculations were run using Density Functional Theory (DFT), Time-Dependent DFT (TD-DFT), and dispersion-corrected PM6 in parallel to the experiments to help guide the identification and assignment of NAO aggregates and to improve the general understanding of the results. The theoretical model was initially tested by verifying that CL bilayers can form spontaneously ($\Delta H = -101$ kJ/mol), while interactions between two such bilayers are unfavorable ($\Delta H = +309$ kJ/mol, Supplementary Fig. 5a), as indeed observed experimentally. The insertion of NAO in the CL bilayer is highly favorable ($\Delta H = -427$ kJ/mol) mainly because the polar/negatively charged phosphates are very close to the positive charge of NAO, stabilizing it (Fig. 3a, left side), but also because the non-polar tail of NAO fits the non-polar pocket between two CLs. Most importantly, the presence of NAO in the CL bilayer strongly stabilizes the interactions between two bilayers (Fig. 3a, right side), when compared to the same supramolecular process in the absence of NAO ($\Delta H = +295$ kJ/mol, Supplementary Fig. 5b).

The ZINDO/S model was then used to calculate the absorption properties of NAO as a monomer and aggregate, with the latter adopting inter- or intrabilayer geometries (Fig. 3b). The intrabilayer dimer absorbs at almost the same wavelength as the monomer, whereas the interbilayer absorption dimer is blue-shifted (Fig. 3b). The simulated UV–Vis spectra, together with the experimental, blue-shifted, absorption spectrum of NAO-incorporated lipid vesicles suggest the formation of interbilayer antiparallel H-dimers (Fig. 3b, left structure). DFT and TD-DFT calculations were then used to predict the lowest singlet excited state (S_1) of the interbilayer dimer shown in Fig. 3b. This provides an estimation of the emission wavelength of the excited-state dimer, which can be approximated as an excimer. Note that when an excimer emits (red-shifted) light, it does not decay back to a stable ground state dimer, as assumed here, but to two separated ground-state monomers. However, the TD-DFT calculations provided a rough estimation of the longest emission wavelength (λ_{em}) of the interbilayer H-dimers, where $\lambda_{em} > 647$ nm. This qualitatively agrees with the experimental fluorescence spectra and, more importantly, with the dimeric species observed by FLIM experiments after the insertion of NAO in the bilayer. The theoretical results together with experimental results thus indicate that the presence of negative charges on the phosphate groups hamper the aggregation of the bilayers. However, NAO promotes such bilayer adhesion through its insertion and the formation of antiparallel H-dimers between opposing bilayers.

3.4. Adhesion energy quantification

We next measured the adhesion strength promoted by antiparallel H-dimers by quantifying the adhesion energy in vesicle doublets. From a theoretical point of view, two adhesion regimes have been described depending on the "tension state" of the vesicles [38,39]. The lateral tension serves to reduce the amplitude of the shape fluctuations and thus to increase the adhesion strength [16,40]. In the weak adhesion regime ($E_{adh} \ll 10^{-6}$ J/m^2, $(\kappa/\sigma)^{1/2} \gg R_c$, where R_c is the characteristic size of the contact site, i.e., $\sigma < 10^{-7}$ N/m, taking typical values of $\kappa = 10\, k_BT$), the shape of the vesicles results from the interplay between

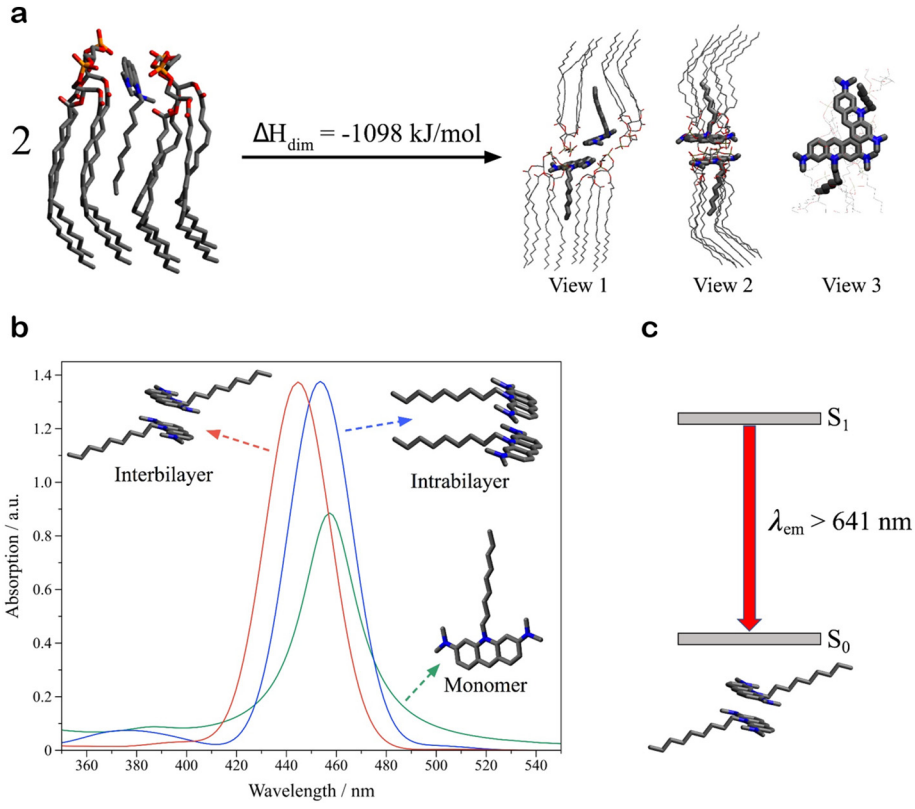

Fig. 3. Semiempirical calculations of calriolipin-NAO interactions. (a) PM6-optimized interbilayer interactions involving two complexes, each containing two negatively charged CL, and one positively charged NAO molecule. Different views of the formed complex are shown. Hydrogen atoms have been omitted for clarity. Color labels: nitrogen (blue), carbon (grey), oxygen (red), phosphor (orange). **(b)** ZINDO/S-simulated absorption spectrum of NAO in monomeric (green line), intrabilayer (blue), and interbilayer (red) form. **(c)** DFT-optimized ground state of NAO in interbilayer form, together with the lowest excited singlet state predicted for the same dimer using TD-DFT. The arrow is a rough estimation of the excimer emission. (For interpretation of the references to color in this figure legend, the reader is referred to the web version of this article.)

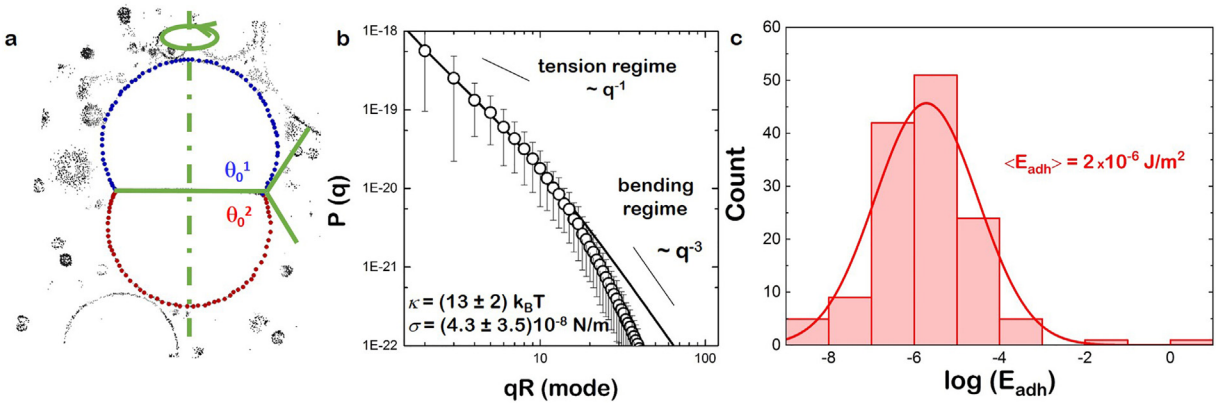

Fig. 4. Quantification of NAO-promoted adhesion. (a) Schematic diagram of two giant vesicles in adhesive contact. Contact angles are denoted by θ_0^i. The vesicle contour was obtained from the pixels with maximum fluorescence intensity (solid circles). The enclosed volume and the total membrane area of each adhering vesicle were measured by integration along their contour, assuming that the shapes were axisymmetric. **(b)** Typical fluctuation spectrum for *E.coli* PLE GUVs. The solid line represents the best fit to the experimental data using Eq. (5). **(c)** Log-normal distribution of adhesion energy obtained from 69 adhesion events. Adhesion energies were calculated by means of Eq. (4).

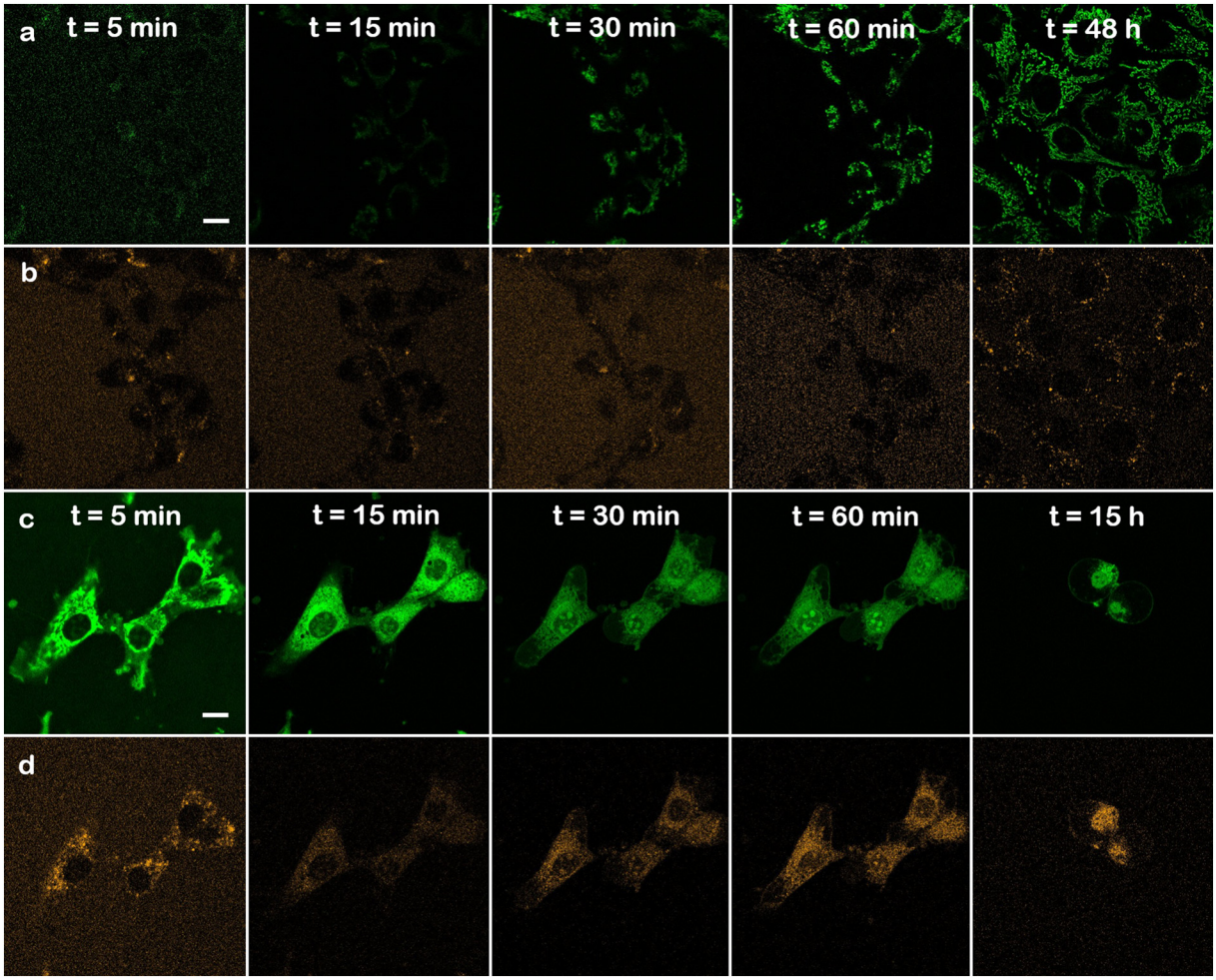

Fig. 5. Interbilayer NAO dimers elicit cytotoxicity in mouse fibroblasts. Confocal fluorescence micrographs (green channel, λ_{exc} = 488 nm and red channel, λ_{exc} = 561 nm) of MEF mitochondria in the presence of 5 nM **(a and b)** and 5 μM of NAO **(c and d)**. At the lower concentration, NAO stains the mitochondrial network (a and b) and does not elicit cell death. At the higher concentration, NAO induces apoptosis (c) and the spectral shift from green to red (d), indicative of the formation of interbilayer NAO dimers (See main text for details). Scale bars are 10 μm.

adhesion and bending energy and the vesicles exhibit a pancake shape. In the strong adhesion regime ($E_{adh} > 10^{-6}$ J/m^2, $(\kappa/\sigma)^{1/2} \ll R_c$, i.e., $\sigma \gg 10^{-6}$ N/m), the bending rigidity is negligible and the vesicles from a shape that is very close to a spherical cap. The appearance of sharp contact angles between GUVs is consistent with a strong adhesion scenario.

Optical microscopy has been shown to be a powerful method for the measurement of adhesion energies between single giant vesicles in the

strong adhesion regime [16,41] (see Materials and Methods, Fig. 4a). The evaluation of the adhesion energy was performed for intermediate concentrations of NAO to avoid multiple adhesion events and vesicle collapse observed at higher concentrations (see Supplementary Fig. 6). We analyzed 69 adhesive events and measured first the surface area A and the volume V of each adhering vesicle. The contact angles and radius, ${\theta_0}^i$ and ${R_0}^i$, between adhering vesicles were then calculated according to Eq. (2) and Eq. (3) respectively.

The estimation of the adhesion energy requires knowledge of the bending modulus of *E. coli* lipids as well, which was obtained from the fluctuation spectra of floppy vesicles. Fig. 4b shows the experimental spectra of *E.coli* PLE GUVs obtained by monitoring the membrane fluctuations at the equatorial plane of the vesicles [19]. The fluctuation spectrum shows a typical dependence with the wavenumber (q), where the amplitudes of the thermal modes become progressively smaller at higher q values (involving a higher curvature). The different power-laws observed rely on the two restoring forces involved in the equatorial fluctuations. At low wavenumbers and below a crossover value, ($q < q_c \approx 1\,\mu m^{-1}$, $q_c = (\sigma/\kappa)^{1/2}$, $q_c R \approx 10$), the membrane fluctuations are restored by the surface tension (σ), their amplitudes scaling as $\sim k_B T/\sigma q$. Above q_c, the amplitude of thermal fluctuations decreases in a regime dominated by the bending rigidity. In this regime, the spectrum scales as $\sim k_B T/\kappa q^3$, allowing the calculation of the bending modulus (κ). On average, we obtained $\kappa = (13 \pm 2)\ k_B T$ for the bending modulus of free *E.coli* PLE GUVs and measured a surface tension of $\sigma = (4.3 \pm 3.5)\ 10^{-8}$ N/m (see Materials and Methods). Using Eq. (4), we finally calculated the adhesion energy with κ, ${\theta_0}^i$ and ${R_0}^i$, and the radius of the adhering membrane segment measured directly from images, R. On average, we found that the adhesion strength was $E_{adh} = (1.8 \pm 0.2)\ 10^{-6}\ J/m^2$ (Fig. 4c).

3.5. Interbilayer NAO dimers elicit cytotoxicity in mouse fibroblasts

In agreement with the seminal literature [5,12], we found that NAO clearly labelled the mitochondria of single living cells when incubated at low concentrations (10 nM). In our case, MEFs were stained with NAO and mitochondria were progressively revealed over time, as shown by the increasing green fluorescence (Fig. 5). Under these conditions, NAO did not induce cell death and the mitochondrial network was not altered after 48 h of incubation (Fig. 5a). Moreover, we only observed the spectral shift of NAO in mitochondria at long incubation times and at particular locations of the mitochondria (Fig. 5b), suggesting a CL accumulation in specific sites of this organelle. At high concentrations, NAO rapidly stains mitochondria both in the green and red channels (Fig. 5c and d). The spectral shift results from the formation of NAO stacking interactions in the presence of mitochondrial CL, since the dye concentration in mitochondria is locally very high. After the first 5 min of incubation, the morphology of the mitochondria starts to change into that of liposomal-shaped membranes and the cells eventually enter apoptosis, as shown by the global morphological changes including blebbing and cell shrinkage (Fig. 5c and d). Fig. 6a shows the GP, Fast FLIM, phasor plots, and phasor color maps of a representative group of living cells after 60 min of treatment with 10 nM NAO. The location of the phasor cluster in the phasor plot determined for the channel #1 FLIM image corresponds to nearly pure NAO monomer molecules. Only NAO red aggregates are observed when cells are treated with high concentrations of NAO (5 μM) (Fig. 6b). At short times, the response of the cells to NAO varies from cell to cell. For those where the adhesion process goes slower, the population of NAO monomers in the mitochondria predominates (blue cursor and blue color in the phasor color map). As adhesion progresses, the population of red NAO aggregates becomes predominant (red cursor and red color in the phasor color map). Note that the excited-state lifetimes of NAO monomer and red aggregates are similar to the GUV values, although the cellular distribution of these species was more heterogeneous.

4. Discussion

Due to strong, intermolecular, van der Waals-like attractive forces between dyes, the self-association of fluorescent probes is a common phenomenon in solution or at liquid–liquid or gas–liquid interfaces. The ability of NAO to form dimers was already reported in the early 1980s [12,35]. From the experimental spectra of NAO in ethanol, Zimmermann et al. built an energy level diagram based on the splitting of the NAO monomer level into two levels corresponding to different NAO dimers with parallel or antiparallel molecular orientation. Hydrophilic interactions between the aliphatic chains of NAO would favor the parallel configuration, while pure acridine orange (AO) dimers or AO-based dyes with shorter alkyl chains would result in antiparallel orientation.

Different molecular matrices for AO molecule dimerization have been reported in the literature [42]. Thus, layer-by-layer (LbL) films of AO dimeric sites predominate over monomeric sites, and the control of H-dimers of AO in LbL films can be achieved by incorporating nano-clay platelets [43]. The formation of parallel AO-based dimers can also be achieved by inserting dyes in mixed stearic acid (SA) monolayers [37]. The formation of parallel H-dimers is tuned in this case by controlling the spacing between the dye molecules via the AO/SA ratio and the orientation of the dipolar moment of the AO-based dye head group by monolayer compression. At collapse pressures, the mixed monolayer leads to an ordered trilayer composed of anisotropic 2D domains of micrometric size. The trilayer structure is stabilized by the strong self-aggregation of antiparallel H-dimers [44]. Here, we present evidence for the formation of antiparallel H-dimers of NAO molecules in lipid bilayers. In our case, the topological scaffold is provided by the hydrophobic moieties from two independent lipid vesicles, which must meet the requirement of including negatively charged lipids in their composition.

The formation of NAO dimers from opposing vesicles promotes strong adhesion between them. Adhesion of flexible GUVs is mediated by nonspecific interactions of physical origin (e.g., electrostatic, hydrophobic, van der Waals) [38] that suppress the repulsive membrane undulations of lipid bilayer counterparts and counterbalance the high energy barrier resulting from the dehydration of the polar headgroups of the lipids as the distance shortens and/or from the entropic repulsion of the headgroups increases. The energy related to short-range interactions between membranes can be estimated from the pressure profile, $P(d)$, of compressed lamellar phases as a function of the interbilayer distance, d [45,46]. The adhesion energy is thus represented by the work of the interbilayer pressure when carrying the membrane from a large distance to the adhesion separation distance, d_{adh}:

$$E_{hyd} = \int_{d_{adh}}^{\infty} P(d)\mathrm{d}d = \int_{d_{adh}}^{\infty} P_0 e^{-\frac{d}{\lambda}}\,\mathrm{d}d = P_0 \lambda e^{-\frac{d_{adh}}{\lambda}} \quad (6)$$

where the amplitude P_0 and the decay length λ depend on the lipid composition and have values of the order of 10^9 Pa and 0.15 nm, respectively. Taking typical values of $d_{adh} =$ 1.7–2.3 nm [47], our estimate for the energy adhesion related to hydration forces is $E_{hyd} \approx 2 \times 10^{-6} - 3 \times 10^{-8}\ J/m^2$. In our case, NAO induces a strong adhesion between vesicles characterized by a high value of the energy density, $E_{adh} \approx 10^{-6}\ J/m^2 > E_{hyd}$, thus high enough to bind the membranes together. Under this strong adhesion regime, vesicles try to maximize their contact area, which induces an increase of the membrane tension up to the lysis tension (~10 mN/m). This picture is supported by the increased orange membrane region over time and the progress of membrane instabilities that promote the collapse of vesicles at high NAO concentration (Supplementary Fig. 6).

In cells, the weak orange fluorescence in the mitochondria of fibroblasts is generated by H-dimers of NAO because the local dye concentration in the mitochondrial membranes is very high. Moreover, a significant fraction of NAO species in cells presents a fluorescence lifetime identical to that found for H-dimers located at the contact

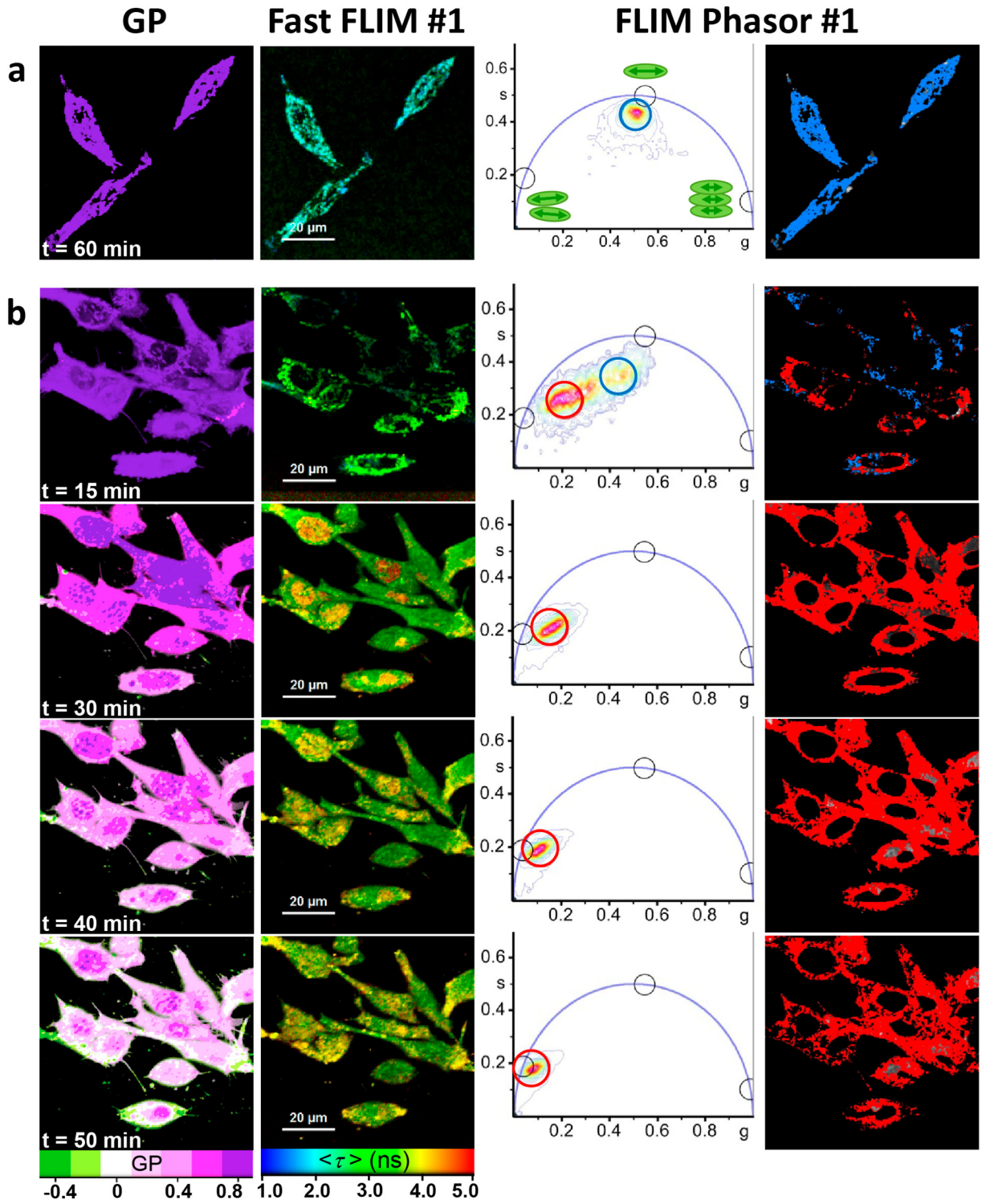

Fig. 6. Spatial distribution of NAO molecular species in mouse fibroblast cells. Basal *XY* sections of representative groups of cells treated with **(a)** 10 nM NAO for 60 min and **(b)** 5 µM NAO at different times. First column: Generalized Polarization images. Second column: Intensity-weighted Fast FLIM images of the same group of cells acquired in the red channel (#1). Third column: Phasor plot showing regions enriched in long-lifetime NAO antiparallel H-dimers (red cursor; as detected in channel #1) and intermediate-lifetime NAO monomers (blue cursor; as detected in channel #1). Black cursors on the phasor plot represent 100% pure NAO species: NAO antiparallel H-dimers (τ = 10 ns), monomeric NAO (τ = 1.8 ns), and self-quenched NAO aggregates (τ = 0.2 ns). Fourth column: Lifetime color maps of NAO molecular species in the red channel (#1). Pixels corresponding to the cluster of phasors enclosed by the colored circles are highlighted on the intensity image using the same color. GP false color green-white-blue violet scale (−0.5, +0.9). Green to blue-violet colors highlight regions showing higher to lower red/green emission ratio for the NAO species, respectively. Fast FLIM rainbow color scale (1–5 ns). λ_{exc} = 850 nm, red channel (#1) FF01 685/40, green channel (#2) FF02 520/35, dichroic filter FF560-Di01 (Semrock, Germany), 1.2 ms/pixel. Scale bar: 20 µm. (For interpretation of the references to color in this figure legend, the reader is referred to the web version of this article.)

region of adhering GUVs. This suggests the existence of antiparallel H-dimers in the mitochondria. Even though the van der Waals attraction could be reduced upon mitochondrial membrane adhesion owing to the presence of membrane proteins and a thicker superficial layer of the outer and inner membranes (7.5 nm thick), the interactions may be favored by the close proximity of both inner and outer membranes, and in particular the membrane patches forming the *cristae* structures. We confirmed the shaping effect of NAO dimers in mitochondrial membranes by electron microscopy and compared it to the case of untreated cells. As shown in Supplementary Fig. 7, incubated mitochondria with a low concentration of NAO (5 nM) displayed a morphology similar to native mitochondria. However, the *cristae* disappeared when NAO was added at high concentrations (5 μM) and double-membrane vesicles appeared. The outer and inner membranes were still visible, forming onion-like structures composed of two, four, or more adhered membranes (Supplementary Fig. 7) [12]. In addition, the dissipation of the mitochondrial membrane potential as a consequence of cell apoptosis [48,49] results in a redistribution of the red-shifted dye within other cell membranes lacking CL in their lipid composition (see Fig. 6).

Supported by all these above considerations, the most likely held view is that antiparallel NAO molecules form a zipper of bonds, where the mechanical adhesion strength relies on the interactions between stacked NAO from opposing bilayers producing membrane remodeling both in model and mitochondrial membranes.

5. Conclusions

In this work we have revealed the mechanism by which the fluorescent dye NAO exhibits cytotoxicity when used at high micromolar concentrations. By conducting FLIM experiments on model membranes and cells, we conclude that cytotoxicity originates from strong interactions between antiparallel H dimers from opposing membranes and thus acting as molecular zippers and promoting their adhesion. The strong adhesion between NAO molecules, $E_{adh} \approx 10^{-6}$ J/m^2, suggests the existence of short-range interactions requiring the close contact between NAO molecules, able to overcome the hydration forces from water molecules bound to the headgroups. The presence of negatively charged lipids is required to provide the optimal supramolecular configuration as suggested by the geometry optimization obtained from semiempirical calculations.

Acknowledgments

This work was supported by the ERC Starting Grant “mitochon” (ERC-StG-2013 338133) and the ERC Proof of Concept “mitozippers” (ERC-PoC-2017 780440), FIS2015-70339-C2-1-R from MINECO (I. L-M. and F.M.), FIS2015-70339-C2-2-R (M.P.L. and C.G.) and S2013/MIT-2807 from the Madrid Regional Government (F.M. and A. G-M.).

References

[1] E. Mileykovskaya, W. Dowhan, R.L. Birke, D.H. Zheng, L. Lutterodt, T.H. Haines, Cardiolipin binds nonyl acridine orange by aggregating the dye at exposed hydrophobic domains on bilayer surfaces, FEBS Lett. 507 (2001) 187–190.
[2] J. Kapuscinski, Z. Darzynkiewicz, Interactions of acridine-orange with double-stranded nucleic-acids - spectral and affinity studies, J. Biomol. Struct. Dyn. 5 (1987) 127–143.
[3] J.M. Petit, A. Maftah, M.H. Ratinaud, R. Julien, N-10-nonyl acridine-orange interacts with cardiolipin and allows the quantification of this phospholipid in isolated-mitochondria, Eur. J. Biochem. 209 (1992) 267–273.
[4] J.M. Petit, O. Huet, P.F. Gallet, A. Maftah, M.H. Ratinaud, R. Julien, Direct analysis and significance of cardiolipin transverse-distribution in mitochondrial inner membranes, Eur. J. Biochem. 220 (1994) 871–879.
[5] U. Erbrich, T. Berthold, H.W. Zimmermann, Über die Wirkung von Acridinfarbstoffen auf die Ultrastruktur von Mitochondrien in HeLa- und LM-Zellen, Histochemistry 76 (1982) 211–218.
[6] A. Maftah, J.M. Petit, M.H. Ratinaud, R. Julien, 10-N nonyl-acridine orange: a fluorescent probe which stains mitochondria independently of their energetic state, Biochem. Biophys. Res. Commun. 164 (1989) 185–190.
[7] A. Maftah, J.M. Petit, R. Julien, Specific interaction of the new fluorescent dye 10-N-nonyl acridine orange with inner mitochondrial membrane. A lipid-mediated inhibition of oxidative phosphorylation, FEBS Lett. 260 (1990) 236–240.
[8] J. Comte, B. Maisterrena, D.C. Gautheron, Lipid-composition and protein profiles of outer and inner membranes from pig heart-mitochondria - comparison with microsomes, Biochim. Biophys. Acta 419 (1976) 271–284.
[9] C. Osman, D.R. Voelker, T. Langer, Making heads or tails of phospholipids in mitochondria, J. Cell Biol. 192 (2011) 7–16.
[10] E. Mileykovskaya, W. Dowhan, Visualization of phospholipid domains in *Escherichia coli* by using the cardiolipin-specific fluorescent dye 10-N-nonyl acridine orange, J. Bacteriol. 182 (2000) 1172–1175.
[11] L.D. Renner, D.B. Weibel, Cardiolipin microdomains localize to negatively curved regions of *Escherichia coli* membranes, Proc. Natl. Acad. Sci. U. S. A. 108 (2011) 6264–6269.
[12] M. Septinus, T. Berthold, A. Naujok, H.W. Zimmermann, Über hydrophobe Acridinfarbstoffe zur Fluorochromierung von Mitochondrien in lebenden Zellen, Histochemistry 82 (1985) 51–66.
[13] L. Mathivet, S. Cribier, P.F. Devaux, Shape change and physical properties of giant phospholipid vesicles prepared in the presence of an AC electric field, Biophys. J. 70 (1996) 1112–1121.
[14] M.J. Hope, M.B. Bally, G. Webb, P.R. Cullis, Production of large unilamellar vesicles by a rapid extrusion procedure - characterization of size distribution, trapped volume and ability to maintain a membrane-potential, Biochim. Biophys. Acta 812 (1985) 55–65.
[15] C. Garcia, A. Losada, M.A. Sacristan, J.F. Martinez-Leal, C.M. Galmarini, M.P. Lillo, Dynamic cellular maps of molecular species: application to drug-target interactions, Sci. Rep. 8 (2018) 1140.
[16] J. Steinkühler, J. Agudo-Canalejo, R. Lipowsky, R. Dimova, Modulating vesicle adhesion by electric fields, Biophys. J. 111 (2016) 1454–1464.
[17] C. Tordeux, J.B. Fournier, P. Galatola, Analytical characterization of adhering vesicles, Phys. Rev. E 65 (2002) 041912.
[18] V.G. Almendro-Vedia, P. Natale, M. Mell, S. Bonneau, F. Monroy, F. Joubert, I. Lopez-Montero, Nonequilibrium fluctuations of lipid membranes by the rotating motor protein F1F0-ATP synthase, Proc. Natl. Acad. Sci. U. S. A. 114 (2017) 11291–11296.
[19] J. Pecreaux, H.G. Dobereiner, J. Prost, J.F. Joanny, P. Bassereau, Refined contour analysis of giant unilamellar vesicles, Eur. Phys. J. E Soft Matter 13 (2004) 277–290.
[20] J. Rezac, P. Hobza, Advanced corrections of hydrogen bonding and dispersion for semiempirical quantum mechanical methods, J. Chem. Theory Comput. 8 (2012) 141–151.
[21] J.P. Perdew, K. Burke, M. Ernzerhof, Generalized gradient approximation made simple, Phys. Rev. Lett. 77 (1996) 3865–3868.
[22] M.C. Zerner, G.H. Loew, R.F. Kirchner, U.T. Muellerwesterhoff, Intermediate neglect of differential-overlap technique for spectroscopy of transition-metal complexes - ferrocene, J. Am. Chem. Soc. 102 (1980) 589–599.
[23] F. Neese, The ORCA program system, Wires Comput. Mol. Sci. 2 (2012) 73–78.
[24] P.M. Oliver, J.A. Crooks, M. Leidl, E.J. Yoon, A. Saghatelian, D.B. Weibel, Localization of anionic phospholipids in Escherichia coli cells, J. Bacteriol. 196 (2014) 3386–3398.
[25] T.H. Haines, N.A. Dencher, Cardiolipin: a proton trap for oxidative phosphorylation, FEBS Lett. 528 (2002) 35–39.
[26] S.E. Horvath, G. Daum, Lipids of mitochondria, Prog. Lipid Res. 52 (2013) 590–614.
[27] C. Stringari, A. Cinquin, O. Cinquin, M.A. Digman, P.J. Donovan, E. Gratton, Phasor approach to fluorescence lifetime microscopy distinguishes different metabolic states of germ cells in a live tissue, Proc. Natl. Acad. Sci. U. S. A. 108 (2011) 13582–13587.
[28] P. Kaewsuya, N.D. Danielson, D. Ekhterae, Fluorescent determination of cardiolipin using 10-N-nonyl acridine orange, Anal. Bioanal. Chem. 387 (2007) 2775–2782.
[29] M. Kasha, H.R. Rawls, M. Ashraf El-Bayoumi, The exciton model in molecular spectroscopy, Pure Appl. Chem. 11 (1965) 371–392.
[30] S. Gadde, E.K. Batchelor, J.P. Weiss, Y. Ling, A.E. Kaifer, Control of H- and J-aggregate formation via host-guest complexation using cucurbituril hosts, J. Am. Chem. Soc. 130 (2008) 17114–17119.
[31] F. Würthner, T.E. Kaiser, C.R. Saha-Möller, J-aggregates: from serendipitous discovery to supramolecular engineering of functional dye materials, Angew. Chem. 50 (2011) 3376–3410 International ed. in English.
[32] S. Chakraborty, P. Debnath, D. Dey, D. Bhattacharjee, S.A. Hussain, Formation of fluorescent H-aggregates of a cyanine dye in ultrathin film and its effect on energy transfer, J. Photochem. Photobiol. A Chem. 293 (2014) 57–64.
[33] D. Chaudhuri, D.B. Li, Y.K. Che, E. Shafran, J.M. Gerton, L. Zang, J.M. Lupton, Enhancing long-range exciton guiding in molecular nanowires by H-Aggregation Lifetime Engineering, Nano Lett. 11 (2011) 488–492.
[34] L. Wang, Y. Shen, M. Yang, X. Zhang, W. Xu, Q. Zhu, J. Wu, Y. Tian, H. Zhou, Novel highly emissive H-aggregates with aggregate fluorescence change in a phenylbenzoxazole-based system, Chem. Commun. 50 (2014) 8723–8726.
[35] M. Septinus, W. Seiffert, H.W. Zimmermann, Über hydrophobe Acridinfarbstoffe zur Fluorochromierung von Mitochondrien in lebenden Zellen, Histochemistry 79 (1983) 443–456.
[36] F. Ito, T. Kakiuchi, T. Nagamura, Excitation energy migration of acridine orange intercalated into deoxyribonucleic acid thin films, J. Phys. Chem. C 111 (2007) 6983–6988.
[37] E. Jiménez-Millán, J.J. Giner-Casares, E. Muñoz, M.T. Martín-Romero, L. Camacho, Self-assembly of Acridine Orange into H-aggregates at the air/water interface: tuning of orientation of headgroup, Langmuir 27 (2011) 14888–14899.
[38] U. Seifert, R. Lipowsky, Adhesion of Vesicles, Phys. Rev. A 42 (1990) 4768–4771.
[39] E. Evans, Entropy-driven tension in vesicle membranes and unbinding of adherent

vesicles, Langmuir 7 (1991) 1900–1908.
[40] R.M. Servuss, W. Helfrich, Mutual adhesion of lecithin membranes at ultralow tensions, J. Phys. France 50 (1989) 809–827.
[41] Y. Sun, C.-C. Lee, H.W. Huang, Adhesion and merging of lipid bilayers: a method for measuring the free energy of adhesion and hemifusion, Biophys. J. 100 (2011) 987–995.
[42] H. Yao, S. Kobayashi, K. Kimura, Self-assembly of acridine orange dye at a mica/solution interface: formation of nanostripe supramolecular architectures, J. Colloid Interface Sci. 307 (2007) 272–279.
[43] J. Bhattacharjee, S.A. Hussain, D. Bhattacharjee, Control of H-dimer formation of acridine orange using nano clay platelets, Spectrochim. Acta A 116 (2013) 148–153.
[44] C. Rubia-Paya, E. Jiménez-Millán, J.J. Giner-Casares, G. Brezesinski, M.T. Martín-Romero, L. Camacho, From two-dimensional to three-dimensional at the air/water interface: the self-aggregation of the acridine dye in mixed monolayers, Langmuir 29 (2013) 4796–4805.
[45] R.P. Rand, V.A. Parsegian, Hydration forces between phospholipid bilayers, Biochim. Biophys. Acta Rev. Biomembr. 988 (1989) 351–376.
[46] R.P. Rand, V.A. Parsegian, Mimicry and mechanism in phospholipid models of membrane fusion, Annu. Rev. Physiol. 48 (1986) 201–212.
[47] S.J. Marrink, O. Berger, P. Tieleman, F. Jahnig, Adhesion forces of lipids in a phospholipid membrane studied by molecular dynamics simulations, Biophys. J. 74 (1998) 931–943.
[48] J.F. Keij, C. Bell-Prince, J.A. Steinkamp, Staining of mitochondrial membranes with 10-nonyl acridine orange MitoFluor Green, and MitoTracker Green is affected by mitochondrial membrane potential altering drugs, Cytometry 39 (2000) 203–210.
[49] J. Jacobson, M.R. Duchen, S.J.R. Heales, Intracellular distribution of the fluorescent dye nonyl acridine orange responds to the mitochondrial membrane potential: implications for assays of cardiolipin and mitochondrial mass, J. Neurochem. 82 (2002) 224–233.